ROYAL SOCIETY
OF CHEMISTRY

COMMUNICATION

Check for updates

An environmentally-benign NaNbO₃ based perovskite antiferroelectric alternative to traditional lead-based counterparts†

Aiwen Xie,[a] He Qi,[a] Ruzhong Zuo, [iD] *[a] Ao Tian,[a] Jun Chen[a] and Shujun Zhang [iD] *[b]

Perovskite-structured antiferroelectric (AFE) materials, which are dominated by PbZrO₃ based solid solutions, are of particular importance owing to their excellent electromechanical properties. The driving force for new development of AFE materials is the result of environmental regulations which require the exclusion of lead components. However, currently reported lead-free AFE materials either show inferior stability or need extremely high driving fields (E_{A-F}) for AFE–FE phase transition. Here we report a new NaNbO₃-based solid solution with a room-temperature stable AFE phase and completely reversible field induced AFE–FE phase transition, possessing a relatively low E_{A-F} of ∼8 kV mm^{-1}, a large repeatable strain of ∼0.29%, and a large polarization difference (P_{max} ∼ 24 μC cm^{-2}, P_r ∼ 0 μC cm^{-2}). The local and average structures were studied by transmission electron microscopy, *in situ* Raman spectrum and synchrotron X-ray diffraction, revealing that the solid solution with ≥16 mol% SrTiO₃ belongs to the *Pnma* space group and exhibits nanoscale stripe domains of ∼55 nm, and reversibly responds to large external electric fields. This makes it a competitive lead-free AFE candidate for future applications of high-power energy-storage capacitors and large-displacement actuators.

1. Introduction

Antiferroelectric (AFE) materials, which possess antiparallel adjacent dipoles, have been actively studied for numerous applications, such as large-displacement actuators or high-power energy-storage capacitors owing to their giant eletro-strains and polarization difference ($\Delta P = P_{max} - P_r$, P_{max}: maximum polarization; P_r: remanent polarization) during electric field

[a] Institute of Electro Ceramics & Devices, School of Materials Science and Engineering, Hefei University of Technology, Hefei, 230009, P. R. China. E-mail: piezolab@hfut.edu.cn

[b] Institute for Superconducting and Electronic Materials, Australian Institute of Innovative Materials, University of Wollongong, NSW 2500, Australia. E-mail: shujun@uow.edu.au

† Electronic supplementary information (ESI) available. See DOI: 10.1039/c9tc05672f

driven reversible AFE to ferroelectric (FE) phase transition, respectively.[1–3] PbZrO₃ (PZ) based compounds are a family of well-established AFE materials exhibiting typical double polarization *versus* electric field (*P–E*) hysteresis loops[4] as well as large repeatable field induced strains being on the order of 0.3–0.8%.[1,5] However, considering the detrimental impact of lead on the environment and human health, lead-free AFE alternatives have attracted much attention in recent years.[6–8] However, none of the lead-free AFE materials reported so far are comparable with PZ based compounds regarding their costs and electrical properties.

NaNbO₃ (NN) is a well-documented lead-free low-cost AFE material compared with AFE AgNbO₃ in the family of niobates. Pure NN at room temperature is commonly referred to as the AFE P phase with an orthorhombic *Pbma* symmetry and exhibits a complex polymorphic phase transition (PPT) sequence (N → P → R → S → T1 → T2 → U) on heating,[9,10] among which the P and R phases are generally recognized as orthorhombic AFEs with different local structures, and the N phase is a low-temperature rhombohedral FE. However, it is difficult to obtain typical double *P–E* loops in polycrystalline NN ceramic samples at room temperature, being ascribed to a similar free energy of the AFE P phase with the FE orthorhombic Q phase ($P2_1ma$),[11,12] which leads to an irreversible P–Q phase transition under an applied electric field. On the other hand, double *P–E* hysteresis loops observed in most NN-based AFE solid-solution ceramics are obviously not repeatable, or strain *versus* electric field (*S–E*) curves are seriously asymmetric, revealing a yet unstable AFE state (becoming an FE state after one field cycle) or a metastable AFE state (an incompletely reversible AFE–FE phase transition), notwithstanding the fact that a lot of effort has been made, including the addition of zirconate perovskites with relatively small tolerance factors (τ), to increase the stability of antiferroelectricity.[13–15] Recent progress was made on the NN–BaZrO₃–CaZrO₃ AFE ceramic with room temperature AFE P phase, which shows a reproducible double *P–E* loop and a large poling strain (S_L ∼ 0.45%).[15] However, the large strain observed during the first field cycle cannot be re-attained

during the following cycles, because the high-field FE phase cannot turn back to its initial AFE state but rather, an intermediate monoclinic AFE phase once the external field is removed. It is believed that simultaneously achieving repeatable P–E and S–E loops with large P_{max} values and high positive strains are prerequisites for the AFE materials aiming at future device applications.

SrTiO$_3$ (ST) is a quantum paraelectric material, which transforms to an antiferrodistortive phase at low temperature.[16] The NN–ST solid solution has been studied with a focus on wet-chemistry processing, crystal chemistry, dielectric energy storage and relaxation behavior,[17–19] but with the absence of exploring its AFE property and potential in actuator applications. Although ST owns a larger tolerance factor than most of the zirconates, the FE phase is not observed at room temperature in NN–ST solid solutions. In contrast, an unexpectedly enhanced stability in the AFE phase was discovered with increasing the concentration of ST in NN. A room temperature stable AFE ceramic with a $Pnma$ space group has been for the first time reported with repeatable double P–E loops ($P_{max} \sim 24$ μC cm^{-2}, $P_r \sim 0$ μC cm^{-2}) and sprout-like S–E curves (positive strain $S_{pos} \sim 0.29\%$, remanent strain $S_r \sim 0\%$ at 13 kV mm^{-1}), demonstrating typical characteristics of traditional AFEs. The reversibility of the AFE–FE phase transition was supported by means of $in\ situ$/$ex\ situ$ synchrotron X-ray diffraction (XRD), Raman spectra and the transmission electron microscopy (TEM) observation, in combination with temperature-dependent dielectric, polarization and strain measurements. This kind of stable NN-based AFE solid solution opens up a new way to replace the traditional PZ-based AFEs for future device applications.

2. Results and discussion

2.1. Adjustment and identification of the phase structure

The dielectric behavior measured during cooling and then heating cycles for $(1 - x)$NN–xST ceramics is shown in Fig. 1a–d and Fig. S1 (ESI†). The pure NN ceramic ($x = 0$) with an AFE orthorhombic P phase at room temperature transforms to an AFE orthorhombic R phase at $T_{\beta H}$ on heating, while goes to an FE rhombohedral N phase at $T_{\alpha C}$ upon cooling (Fig. S1a, ESI†). In addition, the observed thermal hysteresis of dielectric anomalies between cooling and heating cycles indicates the existence of complex first-order PPTs in the studied compositions. The thermal hysteresis of either high-temperature P–R transition (T_β) or low-temperature N–P transition (T_α) obviously decreases with increasing x. However, the latter decreases much faster than the former (for example, $\Delta T_\alpha \sim 95\ °C$ for $x = 0$, but $\Delta T_\alpha \sim 3\ °C$ for $x = 0.05$, see Fig. S1a and b (ESI†); $\Delta T_\beta \sim 56\ °C$ for $x = 0$, $\Delta T_\beta \sim 54.5\ °C$ for $x = 0.05$ and $\Delta T_\beta \sim 50\ °C$ for $x = 0.12$, see Fig. S1a, b, ESI† and Fig. 1a), leading to two dielectric anomalies during heating but only one broad peak during cooling in compositions with higher ST contents, such as $x = 0.14$ and $x = 0.15$. Both the N–P (T_α) and P–R (T_β) PPT temperatures change obviously with increasing x, where T_α slightly increases while T_β rapidly decreases with the addition of ST (for example, $\Delta T_{\alpha C} \sim 20\ °C$ and $\Delta T_{\beta C} \sim -115\ °C$ as
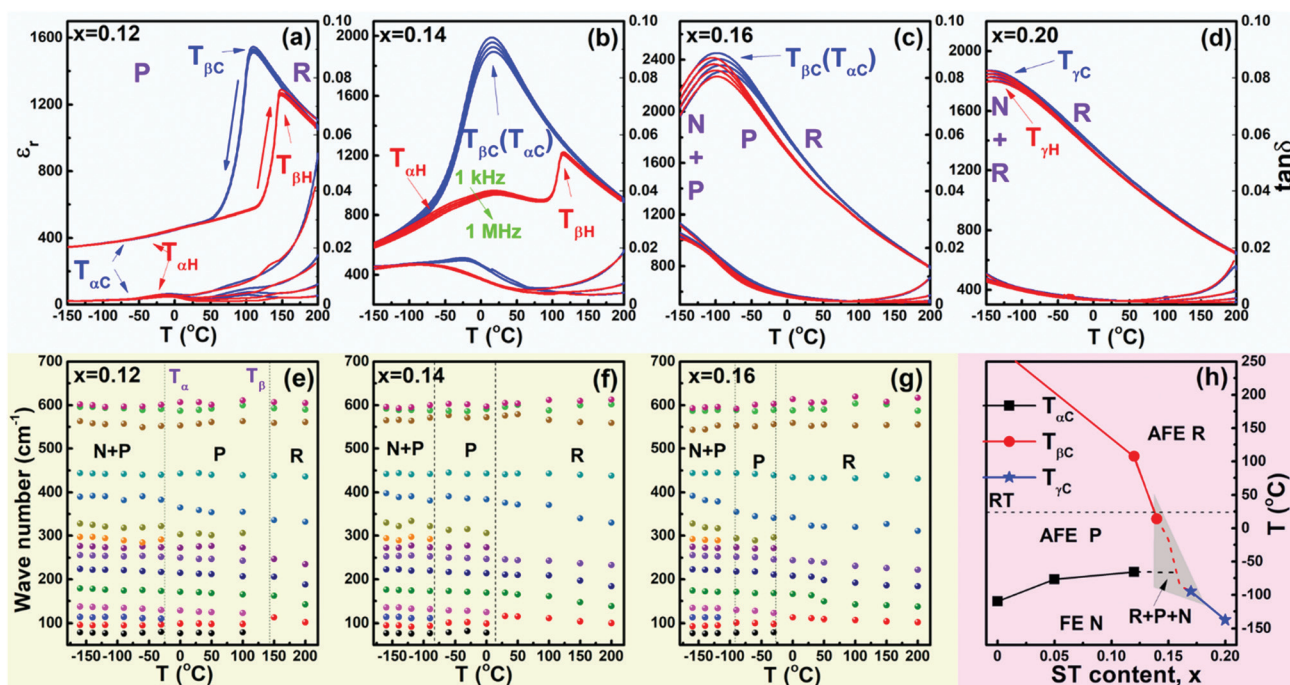

Fig. 1 The dielectric permittivity (ε_r) and dielectric loss (tan δ) as a function of temperature measured on heating and cooling cycles for $(1 - x)$NN–xST ceramics: (a) $x = 0.12$, (b) $x = 0.14$, (c) $x = 0.16$ and (d) $x = 0.2$; temperature dependence of the wave number of a few selected Raman peaks as determined by the multiple peak fitting of the Gauss–Lorentzian function: (e) $x = 0.12$, (f) $x = 0.14$ and (g) $x = 0.16$; (h) the composition–temperature phase diagram obtained from cooling cycles.

x varies from 0 to 0.05). As a result, multi-phases such as N, P and R probably coexist near $T_{\beta C}$ for $x = 0.14$–0.16, but evolve into two phases such as N and R near $T_{\gamma C}$ (N–R PPT) owing to the disappearance of the P phase with increasing x up to 0.17. This is because two separate dielectric anomalies corresponding to the N–P and P–R PPTs can be clearly detected upon heating, suggesting that the AFE orthorhombic P phase zone still exists between the FE rhombohedral N phase and the AFE ortho-rhombic R phase. Moreover, the temperature zone for the AFE R phase shifts rapidly to lower temperatures with the addition of ST, leading to a decrease of N–R PPT temperatures (T_γ) at $x > 0.16$. The variation trends of T_α and T_β shown above strongly indicate that the addition of ST with a larger tolerance factor (τ: 1.002 and 0.967 for ST and NN, respectively) into NN tends to stabilize the AFE phases rather than the FE phases, which seems to be in contrast to the general belief that AFE phase can be stabilized by decreasing τ values in perovskite systems.

The above phase transformation behavior can be further supported by means of Raman spectra and XRD measurements at different temperatures from −160 °C to 200 °C. Raman is an effective method to reveal the local structure transformation with changing temperature. Fig. S2 (ESI†) shows Raman spectra for selected $(1 - x)$NN–xST ceramic samples at different tem-peratures. The spectral deconvolution was performed using the Gaussian–Lorentzian function, and the composition depen-dence of the wave number of the selected Raman peaks is displayed in Fig. 1e–g based on the fitting results. According to the group theory, the P phase of NN ceramics exhibits 60 possible Raman active modes.[20] Owing to the large Nb displace-ment nearly towards the midpoint of the oxygen octahedra edge, a large difference between Nb–O bands can be found. As a result, multiple and separated Raman peaks can be detected at <120 cm^{-1} and 120–300 cm^{-1}, in which the Raman modes mainly originate from the translational modes of Na$^+$ and bending modes of Nb–O bonds, respectively.[21] In contrast to the P phase, the FE N phase exhibits only 13 possible Raman active modes. The P–N phase transition may involve the rear-rangement of the Na$^+$ cations and the tilting of the NbO$_6$ octahedra. Owing to the off-center displacement of Na2 by 0.18 Å and essentially undisturbed Na1 in the P phase, two Raman bands can be detected at ~ 75 cm^{-1} and ~ 95 cm^{-1}. Accompanying the appearance of N phase with only one type of Na and smaller Na–O length, a Raman band at higher wave-numbers (~ 114 cm^{-1}) can be observed. By comparing with the P phase with $a^-b^+a^-$ and $a^-b^-a^-$ NbO$_6$ octahedra tilting, the FE N phase shows a much simpler tilting system by $a^-a^-a^-$, thus causing the change of Raman bands over 120–300 cm^{-1}.[22] Based on Raman spectra, it is revealed that mixed N and P phases instead of a pure N phase can be recognized in the studied compositions and temperature range owing to the diffuse feature of the N–P phase transition. A gradual transfor-mation from the N and P coexistence region to the P dominated phase occurs at around T_α. With further increasing temperature approaching to T_β, an obvious change in both the shape and number of Raman peaks below 300 cm^{-1} can be observed, being associated with the R phase. Nevertheless both P and R

phases are orthorhombic AFE, and the R phase exhibits a much smaller Nb displacement than the P phase.[23] As a result, the difference between Nb–O bond lengths in the R phase is quite small, resulting in the overlapped Raman peaks related to the Nb–O bonds. Moreover, an obvious shift of Raman peaks in the range of 150–400 cm^{-1} to lower wavenumber can be seen with both increasing ST content and temperature, indicating the softening of B–O vibrations due to the weakening of the bonding between B-site cations and oxygen. In addition, the obviously decreased peak intensity at ~ 600 cm^{-1} corresponding to phonon softening of BO$_6$ octahedra can further confirm the decrease of the unit cell polarity. Of particular interest is that a decline of the Raman peak intensity at ~ 600 cm^{-1} can also be observed with increasing x from 0.12 to 0.16, as shown in Fig. S2 (ESI†), suggesting that the decreased unit cell polarity induced by ST addition may be responsible for the enhanced AFE stability in NN–ST solid solution.[7,24] Based on these, a compressed tempera-ture range for the P phase zone can be obviously seen with increasing ST content, such that a single dielectric peak corres-ponding to the N–R phase transition occurs starting at $x = 0.17$, as observed in Fig. S1d (ESI†). Moreover, the Raman results also clearly indicate that a pure AFE R phase appears at room temperature as $x \geq 0.16$. By comparison, the $x = 0.14$ ($x = 0.15$ also) ceramic sample should be composed of P and R phases around room temperature. The evolution of the phase structure with temperature for $x = 0.14$ can be further illu-strated by the Rietveld refinement. $R3c$, $P4bm$, $Pnma$, $Ccmm$, $P2_1ma$, and $P2_1$ space groups and their mixtures were attempted for each XRD diffraction line,[11] and the best fitting results are shown in Fig. S3 and Table S1 (ESI†) with the reliability factor of weighted patterns (R_{wp}), the reliability factor of patterns (R_p) and the goodness-of-fit indicator (χ^2) in the range of 8.29–9.41%, 6.72–7.55% and 1.61–1.86, respectively, indicating that the agreements from the selected models are satisfactory. It can be seen that the N and P coexisted phase between −160 °C and −120 °C evolves into a single P phase between −60 °C and 0 °C and then changes to an AFE R dominated phase around room temperature. According to the above analysis, the composition-structure phase diagram can be depicted using the PPT temperatures on cooling, as shown in Fig. 1h. The room tem-perature phase structure of different compositions can be further identified through the Rietveld refinement on full profiles of XRD patterns, as shown in Fig. 2 and Table S2 (ESI†). The fitting results indicate that the room temperature phase structure gradually changes from the coexisted P and Q phases at $x \leq 0.1$ to a pure AFE P phase at $x = 0.11$–0.13, and then to a P–R phase coexistence at $x = 0.14$–0.15 and finally to a pure R phase at $x \geq 0.16$. Accompanying the composition induced phase transition, an obvious change of octahedral tilting can also be found, as shown in the inset of Fig. 2.

2.2. Achieving electric field induced reversible AFE–FE phase transition

It is of great interest to understand the switching characteristics of AFE phases in response to applied electric fields not only for evaluating its application potential but also examining its phase
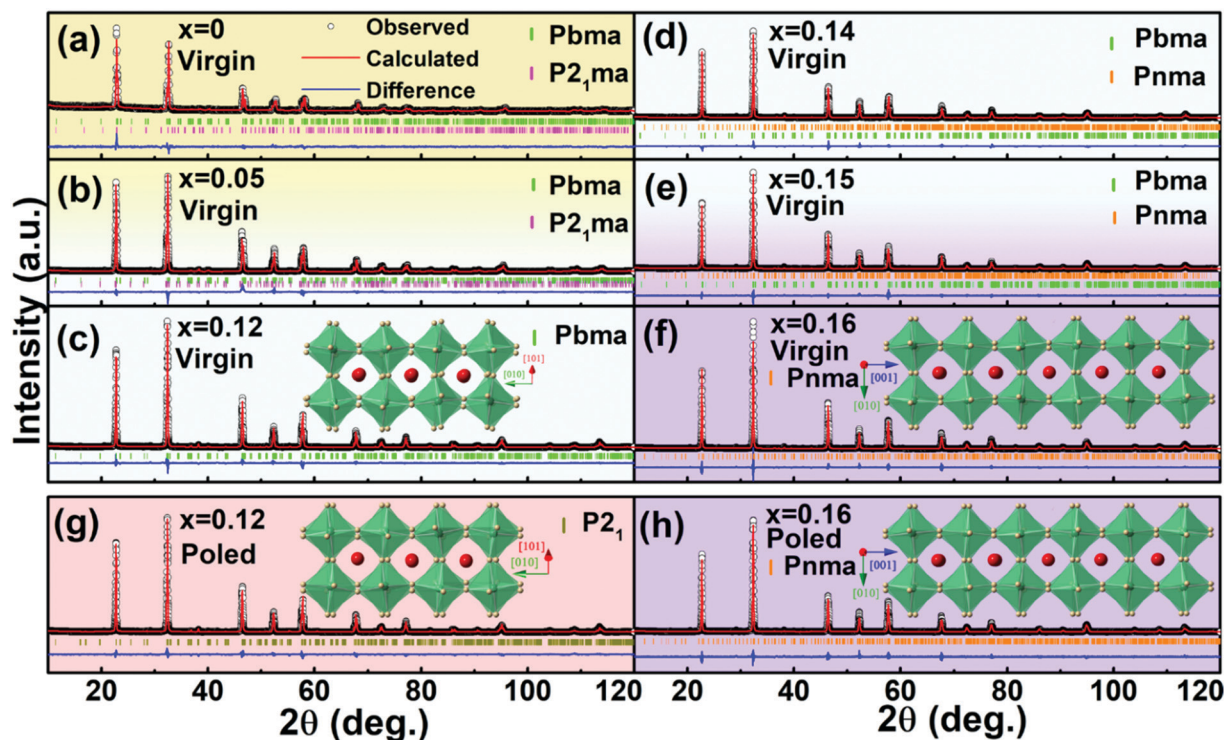
This journal is © The Royal Society of Chemistry 2019

J. Mater. Chem. C, 2019, **7**, 15153–15161 | **15155**

Fig. 2 Rietveld refinement plots of conventional XRD patterns for representative $(1 − x)$NN−xST ceramic powders. The insets are the corresponding crystal structure models.

stability, as shown in Fig. 3 and Fig. S4 (ESI†). It is clear that the AFE P phase irreversibly transforms into FE Q phase after the first electric field cycle for compositions with $x \leq 0.1$, as manifested by a square P–E loop in the following cycles (Fig. S4, ESI†), which conforms to the assumption that the P and Q coexist. The irreversible AFE–FE phase transition also induces a quite large difference in S_L between the first and following cycles. However, for compositions with $0.11 \leq x < 0.14$, the double P–E hysteresis loops with good repeatability, together with the inconsistency observed in sprout-like S–E curves between the first and following cycles, clearly suggests an incompletely reversible AFE to FE phase transition. This is due to the fact that the initial AFE orthorhombic P phase cannot be automatically recovered from the high-field FE phase but transforms to another AFE phase (monoclinic with $P2_1$ space group, see below) after polarization,[15] leading to a relatively small strain step on the left side of the bipolar S–E curve compared with the coexisted P–Q phases. Although the oriented AFE domain morphology may cause small irreversible strain,[4] the structure refinement results of the poled ceramic powder with $x = 0.12$ support the formation of a new metastable AFE phase with $P2_1$ space group (see Fig. 2g). On the other hand, for $0.14 \leq x \leq 0.15$ compositions with coexisted P and R phases, both double P–E hysteresis loops ($P_{max} \sim 23$–25 μC cm^{-2} and $P_r \sim 3$–7 μC cm^{-2} at $x = 0.14$–0.15) and sprout-like S–E curves ($S_L \sim 0.29\%$) without negative strains can be detected, exhibiting good repeatability. This demonstrates that not only remaining AFE orthorhombic P phase but also the AFE orthorhombic R phase can reversibly transform to an FE phase. As $x \geq 0.16$, pure AFE orthorhombic
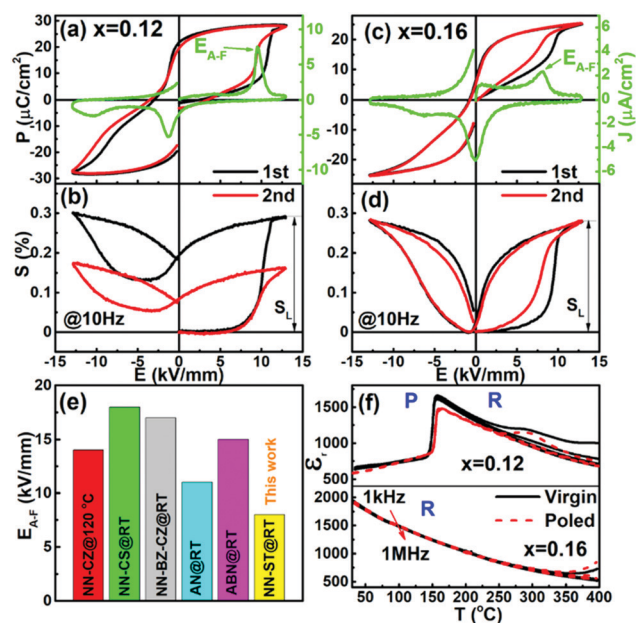

Fig. 3 P–E loops, corresponding J–E curves and S–E curves of (a and b) $x = 0.12$ and (c and d) $x = 0.16$ ceramic measured during different electric cycles at 10 Hz; (e) a comparison of the E_{A-F} values for various recently reported lead-free AFE ceramics, NN–CZ: 0.95NaNbO$_3$–0.05CaZrO$_3$,[13] NN–CS: 0.96NaNbO$_3$–0.04CaSnO$_3$,[14] NN–BZ–CZ: 0.91NaNbO$_3$–0.06BaZrO$_3$–0.03CaZrO$_3$,[15] AN: AgNbO$_3$,[7] ABN: Ag$_{0.97}$Bi$_{0.01}$NbO$_3$;[25] (f) the dielectric permittivity as a function of temperature and frequency for virgin and poled $x = 0.12$ and $x = 0.16$ ceramics.

R-phase ceramic was found to exhibit typical characteristics of traditional AFEs.

In addition to a large polarization difference ($P_{max} \sim$ 24 μC cm^{-2}, $P_r \sim 0$ μC cm^{-2}), a repeatable large poling strain of $\sim$0.29% and a relatively low threshold electric field for AFE–FE phase transition ($E_{A-F} \sim 8$ kV mm^{-1}) can be attained at $x = 0.16$ (see the polarization current density *versus* electric field (J–E) curves in Fig. 3a and c), compared with most of the other niobate lead-free AFE ceramics,[7,13–15,25] as shown in Fig. 3e, demonstrating potential advantages for large displacement actuators. It should be noted that the increase of E_{A-F} values with increasing x leads to a decayed strain value and an unopened P–E loop (Fig. S4g and h, ESI†). The slight difference observed in P–E loop for $x \geq 0.16$ samples from that of typical PZ-based AFEs and NN-based AFE with the P phase is thought to be correlated with their dielectric relaxation behavior (see Fig. 1 and Fig. S1, ESI†). Moreover, the above results also indicate that both P and R AFE phases become more stable with increasing ST content. As shown in Fig. 3f, completely repeatable ε_r–T curves further confirm that the initial AFE state and the poled AFE state should be the same for the $x = 0.16$ ceramic with a single AFE R phase at room temperature.

In contrast, an irreversible change caused by electric field in an $x = 0.12$ sample with a pure room temperature AFE P phase makes a difference in ε_r–T curves between virgin and poled samples. This can be further supported by comparing the structure refinement results of virgin and poled sample powders with $x = 0.12$ and $x = 0.16$, as shown in Fig. 2c, f–h and Table S2 (ESI†).

2.3. Domain morphology and local symmetry by TEM

HR-TEM characterization is an effective method to identity AFE phases from the viewpoint of their domain morphology and local structure. As shown in Fig. 4a and b, typical AFE domain morphology with hierarchical domain microstructures for the $x = 0.16$ ceramic sample can be observed along the $[100]_C$ crystallographic direction owing to a combination of cation displacements and modulated oxygen octahedra tilts and twists.[26] Typical stripe domains on the subgrain level, and commensurate modulation stripes of a width of $\sim$2.4 nm within domains can be observed. Compared with typical AFE P phase ($x = 0.12$) with macroscopic domains (see Fig. S5, ESI†),[13,15] the AFE R phase ($x = 0.16$) has extremely small stripe domains of $\sim$55 nm in width, which basically belong to the 90° domains.[13] It is worth
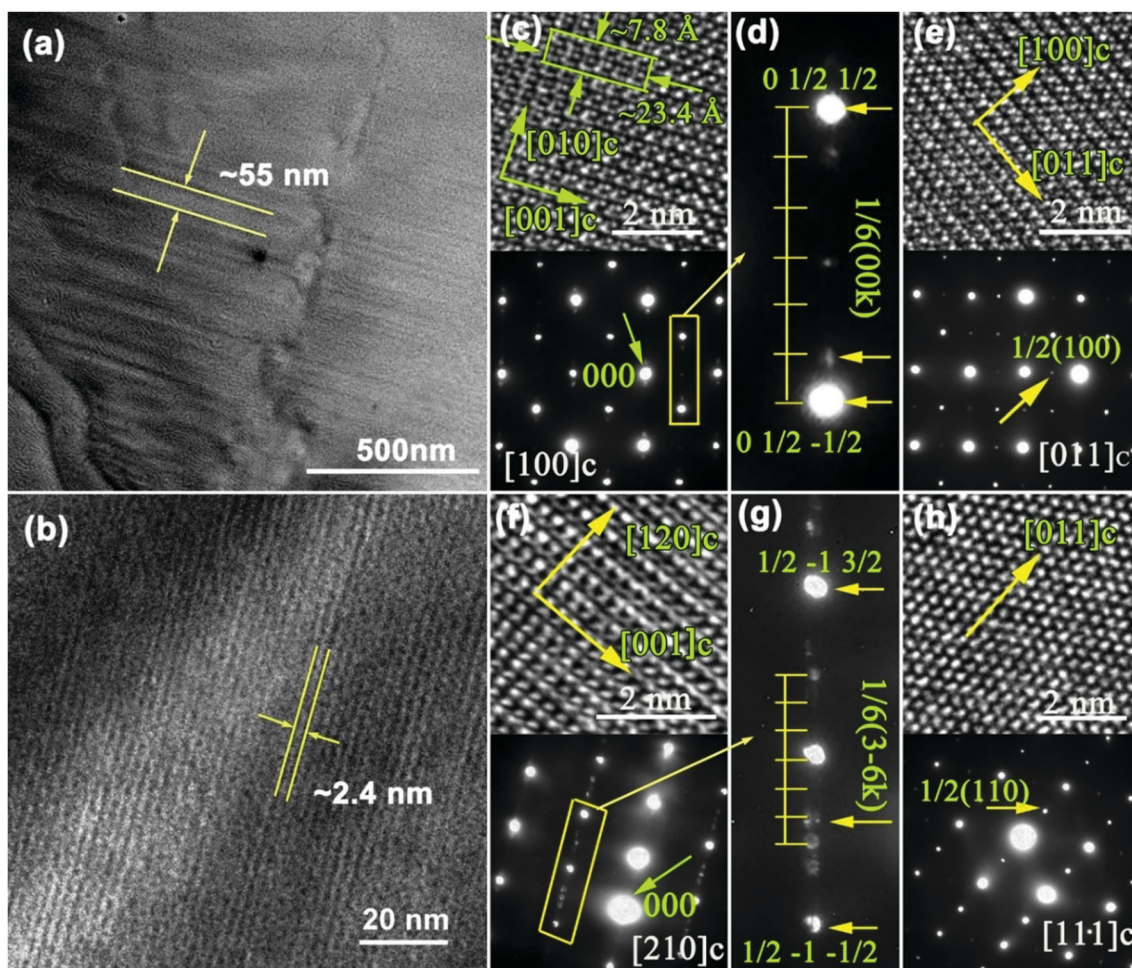

Fig. 4 Room temperature domain structure of the AFE R phase composition. (a) Bright-field TEM image and (b) HR-TEM image of the $x = 0.16$ ceramic along the $[100]_C$ direction; the SAED patterns and the HR-TEM images of lattice fringes along the (c and d) $[100]_C$, (e) $[011]_C$, (f and g) $[210]_C$ and (h) $[111]_C$ directions.

This journal is © The Royal Society of Chemistry 2019

J. Mater. Chem. C, 2019, **7**, 15153–15161 | **15157**

noting that these nanoscale domains are quite different from polar nanoregions in relaxor FEs, in which only weak contrasts can be observed because the elliptical or spherical polar nano-regions usually have a size of <10 nm.[27] The rapid reduction of domain sizes observed in different compositions conforms to the obviously enhanced dielectric relaxation characteristics. Moreover, superlattice diffractions as well as ordered arrange-ment of atoms can be clearly found on both the SAED and HR-TEM image, as shown in Fig. 4c–h. According to the enlarged SAED pictures measured along the $[100]_C$ and $[210]_C$ crystallographic directions in Fig. 4c and f, respectively, the 1/6 type superlattice reflections can be detected in Fig. 4d and g, clearly confirming a commensurate modulated phase with six-fold unit cell along the $[001]_C$ crystallographic direction. The appearance of superlattice diffraction should be mainly related to the cation antiparallel displacements and/or oxygen octahedra tilts. For normal FEs and relaxor FEs, 1/2 type or even no superlattice diffraction can be usually observed owing to the absence of antiparallel displacements. Yet, superlattice diffraction for AFEs is formed by a combination of cation antiparallel displacements and modulated oxygen octahedra tilts. $1/n$ type superlattice spots with $n > 2$ or even satellite

spots with non-integer thus can be found in AFEs. 1/6 type superlattice spots are a specific character for the AFE R phase in NN, because AFE P and incommensurate AFE phases show 1/4 type (see Fig. S5, ESI†) and unequally spaced superlattice spots, respectively, and the non-AFE phases in NN show 1/2 type or no superlattice spots. Combined with XRD results, the lattice parameters of AFE R phase are about 7.82 Å × 7.83 Å × 23.51 Å (see Fig. 4c and Table S2, ESI†), which is 2 × 2 × 6 of the basic perovskite unit cells (~3.9 Å). This can be directly understood by the crystal structure model shown in Fig. 2f. Complex octa-hedral tilting of $a^-b^+c^*$ ($c^* = A0CA0C$) can be identified, where the superscripts + and − stand for the same tilt and the opposite tilt that the successive octahedra along an axis have, respectively, and C, 0 and A denote clockwise, zero and anti-clockwise, respectively.[28] 1/2 type superlattice spots caused by the a^- and b^+ octahedral tilting can also be observed along the $[011]_C$ and $[111]_C$ directions, as shown in Fig. 4e and h, respectively.

2.4. Local and average structures and their responses to electric field

In order to further reveal the stability of AFE R phase from the point of view of local structure, *in situ* Raman spectra for the
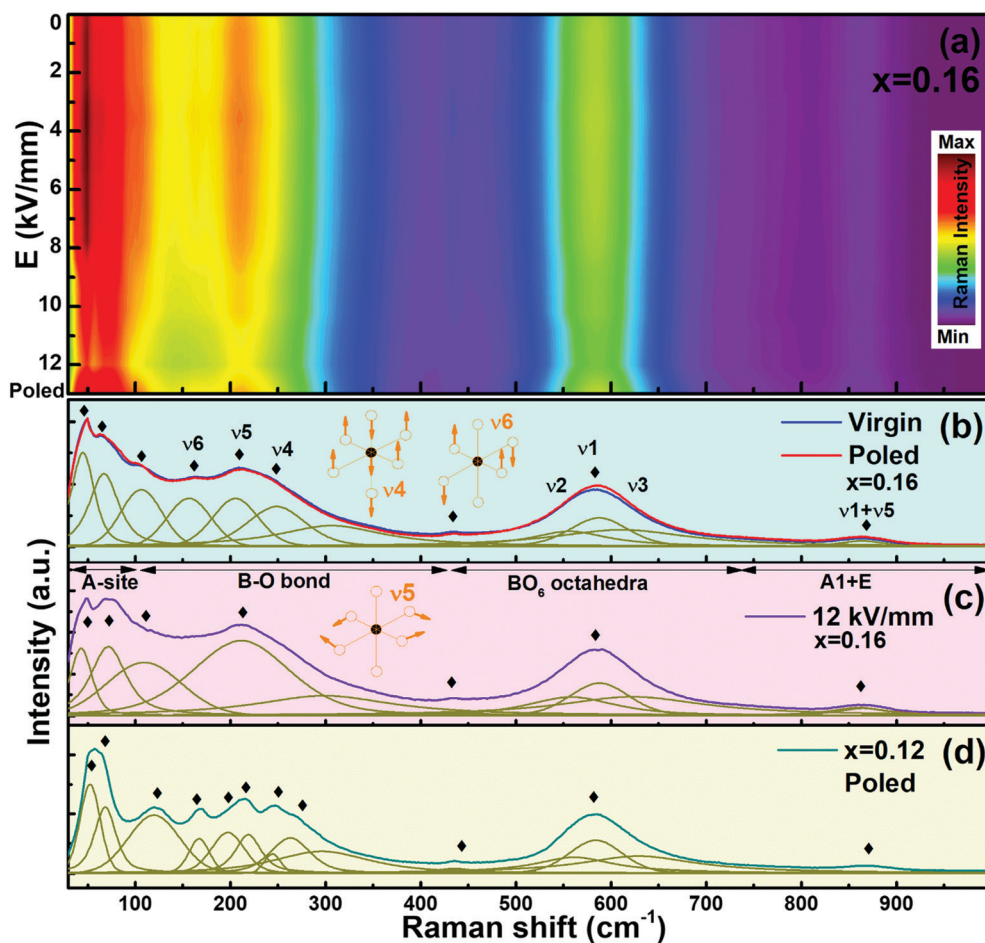

Fig. 5 (a) Evolution of Raman spectra with changing external electric field; a representative spectral deconvolution into Gaussian–Lorentzian-shape peaks for the $x = 0.16$ ceramic under different electric fields: (b) virgin state, poled state and (c) 12 kV mm^{-1}; (d) the Raman spectra for the poled $x = 0.12$ sample. The insets are the schematic representations of $\nu4-\nu6$ bending modes of NbO_6 octahedra.

15158 | *J. Mater. Chem. C*, 2019, **7**, 15153–15161

This journal is © The Royal Society of Chemistry 2019

x = 0.16 composition were measured under various electric fields, as shown in Fig. 5. Minimal change of the multiple peak feature related to the AFE R can be observed until the applied electric field approaches 8 kV mm^{-1}, as shown in Fig. 5a. An additional Raman mode associated with the vibration of A-site cations at ~80 cm^{-1} as well as the disappearance of the Raman mode at ~65 cm^{-1}, and the $\nu4$ and $\nu6$ vibrations relating to the bending modes of NbO$_6$ octahedra, can be found at E > 8 kV mm^{-1}, as clearly reflected on the deconvolution of Raman spectra in Fig. 5b and c. The formation of an AFE R phase occurs by the BO$_6$ octahedra tilt and the antiparallel displacement of B-site cations from the paraelectric cubic structure. When a strong electric field is applied, both A and B-site cations tend to shift along the same axis. Moreover, the change of octahedral tilting system and phase structure might occur simultaneously. The gradually decreased intensity of the Raman peak at ~65 cm^{-1} and the appearance of a new Raman peak at ~80 cm^{-1} clearly reflect the change in the displacement direction of the A-site cations owing to the variation in the oxygen octahedra tilting (might relate to the loss of antiphase tilting). Above 8 kV mm^{-1}, the decrease in intensity and the disappearance of Raman modes at ~170 cm^{-1} and ~250 cm^{-1} (*i.e.*, $\nu6$ and $\nu4$ vibrations), both of which are unique to the orthorhombic phase essentially in NN ceramic as indicated in the insets of Fig. 5b,[22] indicate a gradual transition into a rhombohedral or monoclinic phase. After the removal of the applied electric field, the Raman spectrum is almost in coincidence with that of the virgin sample as shown in Fig. 5b, but being distinctly different from the multi-peak feature of the AFE monoclinic phase for the poled x = 0.12 sample with a $P2_1$ space group (see Fig. 5d and 2g), indicating a complete recovery of the initial AFE R phase in terms of its local structure.

For better understanding the structural origin of the reversible large strains in the AFE R phase, *in situ* synchrotron XRD results of (200)$_C$ and (220)$_C$ reflections under different electric field conditions for the x = 0.16 composition are shown in Fig. 6a. An orthorhombic phase with a typical (200)$_C$ doublet and a (220)$_C$ triplet can be seen in the fresh sample. As an electric field of 8 kV mm^{-1} is applied, the intensity of the (002)$_O$ and (20−2)$_O$ diffraction peaks increases, indicating an obvious non-180° AFE orthorhombic domain reorientation along the electric field direction. At E = 10 kV mm^{-1}, additional reflections on both (200)$_C$ and (220)$_C$ can be observed, indicating the formation of an FE monoclinic phase under a high field. An obvious texture of the induced FE monoclinic phase corresponding to non-180° FE domain switching can be detected with further increasing the electric field magnitude (up to 13 kV mm^{-1}). After the electric field is removed, both (200)$_C$ and (220)$_C$ diffraction peaks basically turn back to their initial states in either peak shape or intensity, indicating that field induced AFE to FE phase transition is reversible in the x = 0.16 sample. Lattice strains (S_{latt}) can be achieved according to the peak shift along the non-polar axes between poling and virgin states.[29] The volume strain (S_v) can be obtained from the transverse (S_t) and longitudinal strain (S_l) in Fig. 6b using the equation: $S_v = S_l + 2S_t$. In addition to S_{latt} and $S_v/3$, the rest of the
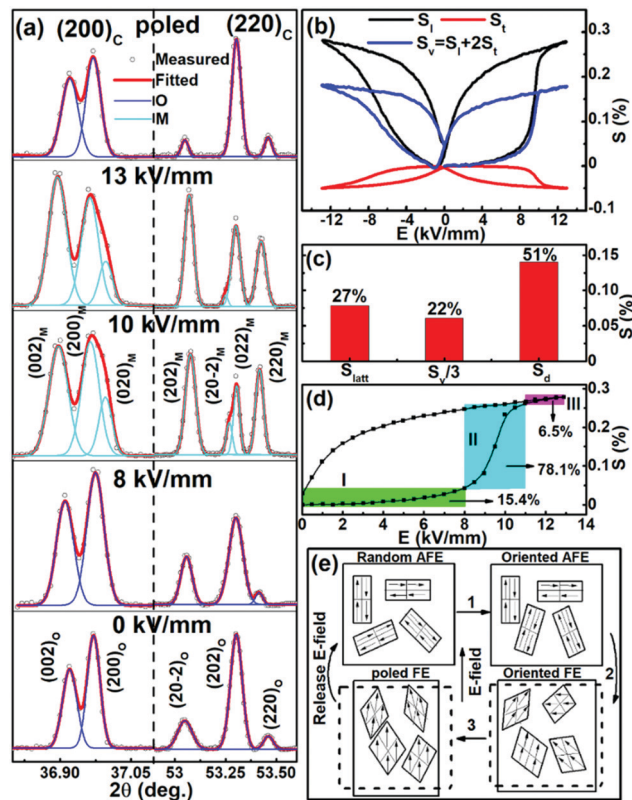

Fig. 6 (a) Evolution of (200)$_C$ and (220)$_C$ reflections under different field conditions for the x = 0.16 sample; (b) the longitudinal strain S_l, transverse strain S_t and the corresponding volume strain S_v measured at 10 Hz for the x = 0.16 ceramic, and (c) the S_{latt}, $S_v/3$ and S_d for the x = 0.16 ceramic; (d) the unipolar strain as a function of the magnitude of the applied electric field for the x = 0.16 ceramic; (e) a schematic diagram of the field induced AFE–FE phase switching process (1: AFE domain texturing, 2: AFE to FE transition, plus FE domain texturing, 3: further texturing of FE domain).

contributions to the poling strain should be from the non-180° domain switching (S_d), as characterized by the variation of diffraction peak intensities in Fig. 6a. The corresponding strain contribution fractions are shown in Fig. 6c, demonstrating a dominant contribution from the non-180° domain switching (S_d ~ 51%) apart from S_{latt} ~ 27% and $S_v/3$ ~ 22%. Fig. 6d shows a unipolar strain loop of the x = 0.16 ceramic. It can be seen that the evolution of strain during the increase of electric field can be roughly divided into three stages. The two stages corresponding to the low (E < 8 kV mm^{-1}, Part I) and high fields (>11 kV mm^{-1}, Part III) make a relatively small strain contribution from the electrostriction effect and the non-180° domain switching. By comparison, a dominant strain contribution (~78.1%) occurs over an electric field of $8 \leq E \leq 11$ kV mm^{-1} (Part II), in which the ramp up of the strain with electric field accounts for the large volume effect during the field induced AFE–FE phase transition. Considering the actual volume strain is only ~22% of the total poling strain, the AFE–FE phase transition and the texture of the FE monoclinic domains (namely non-180° FE domain switching) should occur simultaneously at Part II. The evolution of the diffraction peaks (Fig. 6a) and the unipolar strain (Fig. 6d) provides a general

This journal is © The Royal Society of Chemistry 2019

J. Mater. Chem. C, 2019, 7, 15153–15161 | 15159

description of the domain morphology evolving with applied electric fields, as schematically presented in Fig. 6e. It can be seen that the domain reorientation occurs during the entire electric field cycle, involving the AFE and FE non-180° domain switching in succession. Therefore, *in situ* synchrotron XRD measurements provide additional evidence of the reversible AFE–FE phase transition from the aspect of average structure. In addition, large volume effects accompanying rapid increase of strains observed in the $x = 0.16$ sample show typical characteristics of lead-based AFE ceramics.

3. Conclusions

In summary, the addition of ST with a larger τ was surprisingly found to effectively stabilize the AFE phase in NN-based solid solution, which is closely associated with the decreased unit cell polarity induced by the ST. A completely reversible electric field induced AFE to FE phase transition (repeatable double *P–E* and sprout-like *S–E* loops) was for the first time realized at room temperature in the NN-based AFE orthorhombic R phase ($x \geq 0.16$), in stark contrast to the traditional AFE ortho-rhombic P phase, as confirmed by the XRD refinement, TEM and *P/S–E* loop measurements. The *in situ* Raman spectra and synchrotron XRD results further confirm that the electric field induced FE monoclinic phase can completely switch back to the initial AFE R phase after removing the applied electric fields, based on the local and average structures respectively. Moreover, the ramp up of the strain above a field of 8 kV mm^{-1} was ascribed to the large volume effect between the AFE orthorhombic R phase and FE monoclinic phase. The achieve-ment of the large poling strains (0.29% at a relatively low $E_{A-F} \sim 8$ kV mm^{-1}), repeatable *P/S–E* loops and large polariza-tion difference ($P_{max} \sim 24$ μC cm^{-2}, $P_r \sim 0$ μC cm^{-2}) in the AFE R phase would open up a new possibility of NN-based lead-free AFE ceramics for replacing traditional Pb-based AFE com-pounds in the field of high-displacement actuators and high power energy-storage capacitors.

4. Experimental section

Ceramic fabrication

$(1 - x)$NN–xST ($0 \leq x \leq 0.2$) solid solution ceramics were prepared *via* a solid-state reaction method using high-purity Na_2CO_3, Nb_2O_5, $SrCO_3$ and TiO_2 (AR, Sinopharm Chemical Reagent Co., Ltd, CN) as raw-materials. The powders were mixed thoroughly in ethanol using zirconia balls for 10 h according to their nominal compositions. The mixture was ball-milled again for 10 h after calcination at 900 °C for 5 h. The as-pressed disk samples were sintered at 1300–1340 °C for 2 h in air. Silver paste was painted on major sides of the polished samples and then fired at 550 °C for 30 min to form electrodes.

Dielectric measurements

The temperature and frequency dependent dielectric properties were measured by an LCR meter (Agilent E4980A, Santa Clara, CA)

and a broad frequency dielectric spectrometer (Concept 80, Novocontrol Inc, Germany) at a heating and cooling rate of 3 °C min^{-1}.

In situ Raman spectra

Temperature dependent Raman spectra were collected on well-polished pellets by 532 nm laser excitation using a Raman spectrometer (LabRam HR Evolution, HORIBA JOBIN YVON, Longjumeau Cedex, France). For measuring Raman spectra under different electric fields, the laser beam was always focused on the same grain at the side of the specimen by applying external electric fields on the major side of the sample perpendicular to the direction of the laser beam.

XRD

A conventional powder X-ray diffractometer (D/Max-RB, Rigaku, Tokyo, Japan) with Cu Kα radiation (λ = 1.5418 Å) under acceleration conditions of 40 kV and 30 mA was used to detect the crystal structure at different temperatures. The diffraction data were collected at steps of 0.01° of 2θ over the range of 10–120°, at a scanning speed of 5° min^{-1}. The powder XRD data were quantitatively analyzed by the Rietveld refinement using GSAS software. Powders for the XRD measurements were prepared after gentle grinding of the as-sintered and poled pellets in ethanol. Electric poling was carried out on the pellets by applying a dc field of 10 kV mm^{-1} for 15 min at room temperature.

Ferroelectric and electrostrain measurements

The *P–E* and *S–E* curves were measured by using a ferroelectric measuring system (Precision multiferroelectric, Radiant Techno-logies Inc., Albuquerque, NM) with an accessory laser interferometer vibrometer (AE SP-S 120E, SIOS Mebtechnik, GmbH, Ilmenau, Germany). To estimate the electric field-induced volume changes, *S–E* curves were measured along the directions being parallel and perpendicular to the poled direction simultaneously.

TEM

The domain morphology observation, selected area electron diffraction (SAED) and high-resolution (HR) atomic imaging were performed on a field-emission TEM (FE-TEM, JEM-2100F, JEOL, Japan) with double tilting stage operated at 200 kV. For TEM examination, samples were first mechanically polished to a thickness of ~ 20 μm and then Ar ion-milled in a Precision Ion Polishing System (PIPS, Model 691, Gatan Inc., Pleasanton, CA, USA) at 5 kV. All specimens were annealed at 80 °C at a heating and cooling rate of ~ 0.5 °C min^{-1} for at least one day to release the mechanical stress before the observation.

In situ XRD

The *in situ* XRD measurements on disk samples were carried out at beamline 14B1 (λ = 1.2398 Å, 10 keV) at Shanghai Synchrotron Radiation Facility (SSRF) through θ–2θ step-scans using a Huber 5021 six-circle diffractometer with a NaI scintillation detector. For high-resolution XRD measurements, gold electrodes were sputtered onto both well-polished sides of the ceramic disk.

15160 | *J. Mater. Chem. C*, 2019, **7**, 15153–15161

This journal is © The Royal Society of Chemistry 2019

Conflicts of interest

Acknowledgements

References

1 K. Uchino, *Jpn. J. Appl. Phys.*, 1985, **24**, 460.

2 W. Y. Pan, C. Q. Dam, Q. M. Zhang and L. E. Cross, *J. Appl. Phys.*, 1989, **66**, 6014.

3 H. S. Wang, Y. C. Liu, T. Q. Yang and S. J. Zhang, *Adv. Funct. Mater.*, 2019, **29**, 1807321.

4 S. E. Park, M. J. Pan, K. Markowski, S. Yoshikawa and L. E. Cross, *J. Appl. Phys.*, 1997, **82**, 1798.

5 R. P. Brodeur, K. W. Gachigi, P. M. Pruna and T. R. Shrout, *J. Am. Ceram. Soc.*, 1994, **77**, 3042.

6 X. L. Tan, C. Ma, J. Frederick, S. Beckman and K. G. Webber, *J. Am. Ceram. Soc.*, 2011, **94**, 4091.

7 L. Zhao, Q. Liu, J. Gao, S. J. Zhang and J. F. Li, *Adv. Mater.*, 2017, **29**, 1701824.

8 G. O. Jones and P. A. Thomas, *Acta Crystallogr., Sect. B: Struct. Sci.*, 2002, **58**, 168.

9 J. Koruza, J. Tellier, B. Malič, V. Bobnar and M. Kosec, *J. Appl. Phys.*, 2010, **108**, 113509.

10 S. K. Mishra, R. Mittal, V. Y. Pomjakushin and S. L. Chaplot, *Phys. Rev. B: Condens. Matter Mater. Phys.*, 2011, **83**, 134105.

11 S. K. Mishra, N. Choudhury, S. L. Chaplot, P. S. R. Krishna and R. Mittal, *Phys. Rev. B: Condens. Matter Mater. Phys.*, 2007, **76**, 024110.

12 K. E. Johnston, C. C. Tang, J. E. Parker, K. S. Knight, P. Lightfoot and S. E. Ashbrook, *J. Am. Chem. Soc.*, 2010, **132**, 8732.

13 H. Shimizu, H. Z. Guo, S. E. Reyes-Lillo, Y. Mizuno, K. M. Rabec and C. A. Randall, *Dalton Trans.*, 2015, **44**, 10763.

14 J. M. Ye, G. S. Wang, X. F. Chen, F. Cao and X. L. Dong, *Appl. Phys. Lett.*, 2019, **114**, 122901.

15 R. Z. Zuo, J. Fu and H. Qi, *Acta Mater.*, 2018, **161**, 352.

16 J. P. Buban, H. Iddir and S. Öğüt, *Phys. Rev. B: Condens. Matter Mater. Phys.*, 2004, **69**, 180102(R).

17 H. W. Xu, A. Navrotsky, Y. L. Su and M. L. Balmer, *Chem. Mater.*, 2005, **17**, 1880.

18 T. Hungria, M. Algueró and A. Castro, *Chem. Mater.*, 2006, **18**, 5370.

19 M. X. Zhou, R. H. Liang, Z. Y. Zhou, S. G. Yan and X. L. Dong, *ACS Sustainable Chem. Eng.*, 2018, **6**, 12755.

20 Yu. I. Yuzyuk, E. Gagarina, P. Simon, L. A. Reznitchenko, L. Hennet and D. Thiaudière, *Phys. Rev. B: Condens. Matter Mater. Phys.*, 2004, **69**, 144105.

21 K. Kakimoto, K. Akao, Y. Guo and H. Ohsato, *Jpn. J. Appl. Phys.*, 2005, **44**, 7064.

22 K. K. Mishra, V. Sivasubramanian and A. K. Arora, *J. Raman Spectrosc.*, 2011, **42**, 517.

23 I. Lefkowitz, K. Łukaszewicz and H. D. Megaw, *Acta Crystallogr.*, 1966, **20**, 670.

24 Y. Takagi, *Phys. Rev.*, 1952, **85**, 315.

25 Y. Tian, L. Jin, H. F. Zhang, Z. Xu, X. Y. Wei, G. Viola, I. Abrahams and H. X. Yan, *J. Mater. Chem. A*, 2017, **5**, 17525.

26 J. S. Speck, M. De Graef, A. P. Wilkinson, A. K. Cheetham and D. R. Clarke, *J. Appl. Phys.*, 1993, **73**, 7261.

27 D. Fu, H. Taniguchi, M. Itoh and S. Mori, in *Advances in Ferroelectrics*, ed. A. Peláiz-Barranco, InTech, Rijieka, Croatia, 2012, pp. 51–67.

28 M. D. Peel, S. P. Thompson, A. Daoud-Aladine, S. E. Ashbrook and P. Lightfoot, *Inorg. Chem.*, 2012, **51**, 6876.

29 R. Guo, L. E. Cross, S. E. Park, B. Noheda, D. E. Cox and G. Shirane, *Phys. Rev. Lett.*, 2000, **84**, 5423.

This journal is © The Royal Society of Chemistry 2019

J. Mater. Chem. C, 2019, **7**, 15153–15161 | **15161**